A model of finite electrodes in layered biological media: hybrid image series and moment method scheme

Leonid M. Livshitz, Pinchas D. Einziger and Joseph Mizrahi
*Technion, Israel Institute of Technology Haifa 32000, Israel**

The low-frequency electromagnetic field interaction with layered biological tissue is investigated for electrode array excitation. The problem may be reduced into a system of P (number of electrodes) Fredholm integral equations of the first kind for the electrodes' current distribution. We have shown that the kernel (Green's function) of each integral equation can be expressed by image series. This leads to a most effective inversion of the integral equation system via the moment method, since the moment matrix elements can be expressed explicitly by image series. The outlined procedure is simple to implement and allows estimation of the distributions of low-frequency potential, current, field and power within the multilayer tissue. It may serve as a simplified first-order prototype model for realistic biomedical problems where the dependence on the number of electrodes, tissue layers and their electrical properties must be accounted for. The model has been utilized for the calculation of the electrode array impedance matrix, potential fields, intra-muscular current distributions and isometric recruitment curves (IRC). The simulation results indicate that the IRCs are insensitive to the electrodes' size, however, the inclusion of the bone/fascia layer significantly increases the IRC slope. Furthermore, the simulation scheme, which can be readily implemented for the classification, calibration, verification and interpretation of reported numerical and experimental biomedical data, is also applicable in other problem areas such as geophysical prospecting and electrode grounding in power systems.

Keywords: Electrode array, functional electrical stimulation, finite electrode, image series, layered media, moment method

I. INTRODUCTION

Electrode excitation of biological tissue is a well known and fundamental subject (e.g., [1], [2]), related to almost every functional electrical stimulation (FES) application. It is, therefore, quite a surprise to discover that apart from a few elementary models, dealing with either a single finite electrode in infinite space [3],[4] (both make use of Jackson's derivation for circular electrode [5]), [6], or arrays of point electrodes [7],[8], etc., more general electrode models (analytical or numerical) are not reported in the current literature.

Herein, the electromagnetic field interaction with multilayered biological medium is investigated for electrode array excitation. A layered medium may serve as a simplified first-order prototype model for many realistic biomedical problems where the dependence on the number of electrodes, tissue layers and their electrical properties has to be accounted for (e.g., [9]). The proposed computational procedure can be used as a simple tool for producing analytical data for testing numerical subroutines applied to simulate direct (FES) and inverse (bio electromagnetic imaging) problems in biomedical application [10]. The method outlined can also be applied in other disciplines such as geophysical prospecting [11], [12], and electrode grounding in power systems [13], [14].

The problem may be reduced into a system of P (number of electrodes) Fredholm integral equations of the first kind for the electrodes' current distribution. To obtain an easy to implement and effective solution for an arbitrary number of electrodes and layers, we propose an hybrid solution method. This method is based on a theoretical manipulation of a recently proposed rigorous image series expansions scheme [15],[16] and the numerical moment method [17]. To successfully execute the hybrid method the kernel (Green's function) of each integral equation is expressed by image series. This leads to a most effective inversion of the integral equation system via the moment method, since the moment matrix elements can be expressed explicitly by a finite number of image terms and a collective image, using a novel summation loop operator, and closed-form analytic integration. The procedure outlined is simple to implement and allows estimation of the distributions of low-frequency potential, current, field and power within the multilayer tissue, regardless of the number of electrodes and layers.

The hybrid image series and moment method scheme is applied herein for numerical calculations. The simulations are selected to address simple, yet fundamental, concepts associated with electromagnetic field interaction with biological tissues. Thereby, they demonstrate the potential promise of the hybrid scheme which is capa-

*L. M. Livshitz and J. Mizrahi are with Dept. Biomedical Engineering and P. D. Einziger, is with Dept. Electrical Engineering, Technion, Israel Institute of Technology, Haifa, Israel.
Address for Correspondence: Prof. J. Mizrahi Dept. Biomedical Engineering, Technion, IIT, Haifa 32000, Israel, Fax +972 4 8234131; Electronic address: jm@biomed.technion.ac.il

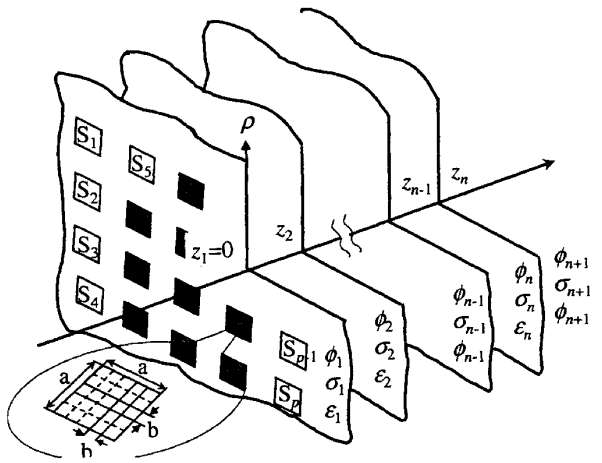

FIG. 1: Physical configuration for layered biological tissue. The medium consists of $n+1$ layers and is excited by a finite electrode array of size P.

ble of efficiently handling 3-D problems in layered media, excited by finite electrode arrays of arbitrary (generally non-planar) configuration. The numerical simulations signify the importance of an appropriate modeling of the tissue layers. Oversimplified models in FES problems, utilizing a reduced number of layers, may result in an inaccurate simulation which greatly deviates from the real problem. Since our hybrid model can effectively handle layered medium problems with any number of layers, a decision whether a particular layer should be included in the model can be accurately made.

II. FORMULATION

A. Problem statement

The physical configuration of our problem, depicted in Fig.1, consists of a stratified biological medium with n boundaries separated between the $n+1$ homogeneous and isotropic layers. An array of P rectangular electrodes is placed in the first layer ($n = 1$). The evaluation of the electrodes' current density distributions and potentials is carried out within the quasistatic (low-frequency) regime. The current density $\mathbf{j}(\mathbf{r})$ and electric field $\mathbf{E}(\mathbf{r})$ are related via [18],

$$\mathbf{j}(\mathbf{r}) = \sigma(z)\mathbf{E}(\mathbf{r}) \tag{1}$$

and

$$\mathbf{E}(\mathbf{r}) = -\nabla\phi(\mathbf{r}), \tag{2}$$

where the potential $\phi(\mathbf{r})$ satisfies Poisson equation

$$\nabla^2\phi(\mathbf{r}) = -i(\mathbf{r})/\sigma(z). \tag{3}$$

The parameter $\sigma(z)$ denotes the piecewise constant conductivity of the medium, i.e.,

$$\sigma(z) = \sigma_i \tag{4}$$

in the i-th layer,

$$z_{i-1} < z < z_i,\ i = 1, 2, ..., n+1,\ z_0 = -\infty,\ z_{n+1} = \infty, \tag{5}$$

and $i(\mathbf{r})$ is the electrodes' current distribution.

We note that $\sigma(z)$ should be replaced by the complex conductivity $\varsigma(z)$

$$\varsigma(z) = \sigma(z) + j\omega\epsilon(z), \tag{6}$$

in every layer for which the inequality $\sigma(z) \gg j\omega\epsilon(z)$ is not satisfied. The parameters $\epsilon(z)$ and ω denote the medium permittivity and the angular (low) frequency of the electrode excitation (assuming time-dependence $e^{j\omega t}$), respectively.

B. Integral equation formulation

The electrodes' current density distribution $i(\mathbf{r})$ can be written explicitly as,

$$i(\mathbf{r}) = \sum_{p=1}^{P} i_p(\mathbf{r}) \tag{7}$$

where $i_p(\mathbf{r})$, the current density distributed on the electrode surface S_p (Fig.1), is given by

$$i_p(\mathbf{r}) = \begin{cases} i_p(\mathbf{r}_p), & \mathbf{r} = \mathbf{r}_p, \quad \mathbf{r}_p \in S_p, \quad p = 1, 2, ..., P, \\ 0, & \mathbf{r} \neq \mathbf{r}_p. \end{cases} \tag{8}$$

Hence, the solution of (3) $\phi(\mathbf{r})$ can be expressed as superposition over all the electrode potentials $\phi_p(\mathbf{r})$,

$$\phi(\mathbf{r}) = \sum_{p=1}^{P} \phi_p(\mathbf{r}), \tag{9}$$

defined via the convolution integral

$$\phi_p(\mathbf{r}) = \frac{1}{\sigma_1} \oint_{S_p} i_p(\mathbf{r}_p) G(\mathbf{r}, \mathbf{r}_p) ds_p. \tag{10}$$

The point-source response $G(\mathbf{r}, \mathbf{r}_p)$, which can be represented in an explicit closed-form expression known as the image series expansion is discussed in Appendix A.

Assuming that all the P electrode plates (Fig.1) are perfect conductors, i.e., constant potential patches, the potential of each electrode is specified. Hence, equation (10) constitutes a system of P Fredholm integral equations of the first kind for the electrodes' current density distribution $i_p(\mathbf{r}_p)$,

$$V_q = \phi(\mathbf{r}_q) = \frac{1}{\sigma_1} \sum_{p=1}^{P} \oint_{S_p} i_p(\mathbf{r}_p) G(\mathbf{r}_q, \mathbf{r}_p) ds_p,\ q = 1, 2, ..., P. \tag{11}$$

Once system (11) is inverted (Section III), i.e, solved for $i(\mathbf{r})$, $\phi(\mathbf{r})$ the solution of (3) is obtained via (9) and (10). Consequently, the vector fields $\mathbf{E}(\mathbf{r})$ and $\mathbf{j}(\mathbf{r})$ are calculated using (2) and (1), respectively.

C. Electrode array

The total current of each electrode I_p is obtained by integration of the electrode current density distribution $i_p(\mathbf{r}_p)$ over the electrode surface,

$$I_p = \oint_{S_p} i_p(\mathbf{r}_p) ds_p. \tag{12}$$

The uniqueness of the solution of system (11) in conjunction with the superposition principle leads to the following linear relation between the electrode currents and electrode voltages

$$\mathbf{I} = \mathbf{G}\mathbf{V}, \tag{13}$$

or, alternatively, $\mathbf{V} = \mathbf{R}\mathbf{I}$, where $\mathbf{G}$ and $\mathbf{R} = \mathbf{G}^{-1}$ denote the input conductance (admittance) and the input resistance (impedance) $P \times P$ matrices of the electrode array feeding network, respectively. It can be readily shown that the matrices $\mathbf{R}$ and $\mathbf{G}$ are symmetric due to the reciprocity property of $G(\mathbf{r}, \mathbf{r}_p)$, i.e, $G(\mathbf{r}_q, \mathbf{r}_p) = G(\mathbf{r}_p, \mathbf{r}_q)$. Furthermore, all the diagonal elements of both matrices are positive, whereas, the off-diagonal elements are positive for $\mathbf{R}$ and negative for $\mathbf{G}$.

In view of Kirchhoff's current law, the sum of all the electrode currents must be zero,

$$(1, 1, ..., 1)\mathbf{I} = (1, 1, ..., 1)\mathbf{G}\mathbf{V} = 0, \tag{14}$$

i.e. (LHS),

$$\sum_{p=1}^{P} I_p = 0, \tag{15}$$

or, equivalently (RHS),

$$\sum_{p=1}^{P} \alpha_p V_p = 0, \quad \alpha_p = \sum_{q=1}^{P} G_{qp}. \tag{16}$$

This restriction leads to the conclusion that only P-1 of the elements of either the vector $\mathbf{V}$ or the vector $\mathbf{I}$ can be arbitrarily selected. Thus, the remaining P+1 elements of $\mathbf{V}$ and $\mathbf{I}$ are explicitly specified via either (15) or (16), and (13).

The total complex power S, delivered by a P-electrode array, can be expressed in terms of the vector $\mathbf{V}$ and complex conjugate of the vector $\mathbf{I}$,

$$S = \frac{1}{2}\mathbf{V}^T\mathbf{I}^*. \tag{17}$$

Note that for ω=0, $\varsigma(z) = \sigma(z)$ in (6), leading to real input power $S = \mathbf{V}^T\mathbf{I}$.

III. MOMENT METHOD

The integral equation system in (11) can be inverted using the moment method with pulse base for the electrode current distribution and point match for the potential [17]. The discretized electrode potential $\boldsymbol{\phi}$ is a linear transformation of the discretized current density distribution $\boldsymbol{i}$ via $\mathbf{L}$,

$$\boldsymbol{\phi} = \mathbf{L}\boldsymbol{i}. \tag{18}$$

The moment matrix $\mathbf{L}$ is a square matrix specified by its elements ℓ_{mn} (representing the potential at the center of the subsection m due to unit current density distribution on the subsection n), given as,

$$\ell_{mn} = \frac{1}{\sigma_1} \int_{x_n - b/2}^{x_n + b/2} \int_{y_n - b/2}^{y_n + b/2} G(\mathbf{r}_m, \mathbf{r}_n') \mathrm{d}x_n' \mathrm{d}y_n', \tag{19}$$

where $\mathbf{r}_m$ and $\mathbf{r}_n$ represent the location of the observation and source points, respectively. It can be readily verified that the discretization quanta is a square element of size $b \times b$, thus a square electrode of size $a \times a$ contains $N = (a/b)^2$ subdivisions (Fig.1). Hence, a problem involving P identical square electrodes associates with vectors $\boldsymbol{i}$ and $\boldsymbol{\phi}$ of size PN and a moment matrix $\mathbf{L}$ of size $(PN) \times (PN)$. An explicit closed-form expression for the moment matrix element can be obtained by substituting (A.23) and (A.24) from Appendix A in (19) and utilizing the identity,

$$\begin{aligned} f(x, y, z) &= \int^x \int^y \frac{\mathrm{d}x' \mathrm{d}y'}{r'} \\ &= x \ln(y + r) + y \ln(x + r) - z \arctan(xy/zr), \end{aligned} \tag{20}$$

where $r' = (x'^2 + y'^2 + z^2)^{1/2}$. In this derivation we make use of [19],[20], or more efficiently, the symbolic software, *Mathematica* 2.2 (Wolfram Research Corp.). The expression can be reduced into Bancroft's result [21] upon setting z=0. The resultant element ℓ_{mn} is given by,

$$\begin{aligned} \ell_{mn} = \frac{1}{4\pi\sigma_1} [& h(x_m - x_n + b/2, y_m - y_n + b/2, z_m) \\ & - h(x_m - x_n + b/2, y_m - y_n - b/2, z_m) \\ & - h(x_m - x_n - b/2, y_m - y_n + b/2, z_m) \\ & + h(x_m - x_n - b/2, y_m - y_n - b/2, z_m)], \end{aligned} \tag{21}$$

where $h(x, y, z_m)$ is expressed via the loop operator (see Appendix A),

$$\begin{aligned} h(x, y, z) &= f(x, y, z - z') + K_1 f(x, y, z + z') + \\ &+ \coprod_{j=1}^{n-1} \Bigg[\sum_{l_{j-1}=0}^{m_1 + ... + m_j - l_1 - ... - l_{j-2} + 1} \sum_{m_j=0}^{M_j} \\ &\times \binom{m_1 + ... + m_{j-1} - l_1 - ... - l_{j-2} + 1}{l_{j-1}} \\ &\times \binom{m_1 + ... + m_j - l_1 - ... - l_{j-1}}{m_j} (-K_j)^{m_j} \\ &\times K_j^{l_{j-1}} K_n^{m_j - l_{j-1}} (1 - K_j^2)^{m_1 + ... + m_{j-1} - l_1 - ... - l_{j-1} + 1} \\ &\times f(x, y, z + z_j') \Bigg] K_n + \tilde{\Gamma}_1(z, z') b^2. \end{aligned} \tag{22}$$

The last term in the RHS of (22) represents an asymptotic error estimation of ℓ_{mn} due to the truncated image series expansion in (A.23). This collective image term significantly accelerates the image series convergence and the overall algorithm speed.

Note that, the electrode voltages and currents in (13) are related to the discretized electrode potential and current density distribution in (18) via,

$$\boldsymbol{\phi} = \mathbf{UV} = \mathbf{UG}^{-1}\mathbf{I}, \tag{23}$$

and

$$\mathbf{I} = b^2\mathbf{U}^T i, \tag{24}$$

where $\mathbf{U}$ is a $(PN) \times P$ rectangular matrix,

$$U_{ij} = \begin{cases} 1 & \text{if,} \quad 1+P(j-1) \le i \le Pj \\ 0 & \text{otherwise,} \quad i = 1,2,...,PN, \ j = 1,2,...,N. \end{cases} \tag{25}$$

Thus, using (23) equation (18) can be uniquely inverted once either P-1 electrode voltages or electrode currents are specified (Eqs.(14)-(16)). Furthermore, upon utilizing (24) as well, the conductance matrix $\mathbf{G}$ is completely determine via $\mathbf{L}^{-1}$

$$\mathbf{G} = b^2\mathbf{U}^T\mathbf{L}^{-1}\mathbf{U}. \tag{26}$$

IV. ELECTRODE ARRAY EXCITATION OF LAYERED BIOLOGICAL TISSUE NUMERICAL SIMULATIONS

The hybrid image series and moment method scheme that has been outlined in Sections 2 and 3 is applied herein for numerical calculations. The simulations are selected to address simple, yet fundamental, concepts associated with low-frequency electromagnetic field interaction with biological tissues. Thereby, they demonstrate the potential promise of the hybrid scheme that is capable of efficiently handling 3-D problems in layered media excited by a finite electrode array of an arbitrary (generally non-planar) shape.

The method's efficiency is due to three inherent distinct features, namely: 1. The moment matrix elements l_{mn} are expressed explicitly and recursively via the image series expansion combined with an asymptotic truncation error estimation, i.e., finite number of images and a collective image term; 2. The field vectors $\mathbf{E}(\mathbf{r})$ and $\mathbf{j}(\mathbf{r})$ in (2) and (1), respectively, are obtained through explicit (analytic) closed-form differentiation of $\phi(\mathbf{r})$ and $G(\mathbf{r},\mathbf{r}_p)$ in (8), (9) (i.e., term by term differentiation of the image series expansion) which is more accurate and stable than the numerical differentiation that is used in other schemes. 3. Utilization of the complex conductivity of $\varsigma(z)$ in (6), enables the generation of low-frequency $\omega \neq 0$ field data for the layered media rather than the DC component only.

Since, all of the calculations are carried out for the physical configuration depicted in Fig.1 where $z_p = z_1 = 0$, $p = 1,2,...,P$ (z_p is a component of $\mathbf{r}_p = (x_p, y_p, z_p)$, defined in (8)), $\omega = 0$, and $\sigma_1 = 0$ (air layer), the expression for $G_1(\mathbf{r},\mathbf{r}')$ in (A.23) has to be modified in accordance with the identity,

$$\frac{1+K_1}{\sigma_1} = \frac{1-K_1}{\sigma_2}, \quad \lim_{\sigma_1 \to 0} \frac{1+K_1}{\sigma_1} = \frac{2}{\sigma_2}. \tag{27}$$

Furthermore, the simulations are calculated assuming perfect conducting electrode plates discretized as $b = 0.05a$ ($N = (a/b)^2 = 400$) and the following typical FES parameters: $n = 4$, $\sigma_1 = 0$ (air), $\sigma_2 = 0.4$ S/m $(wet\ skin)$, $\sigma_3 = 0.04$ S/m (fat), $\sigma_4 = 0.7$ S/m $(muscle)$, $\sigma_5 = 0.07$ S/m $(bone/fascia)$, $z_1 = 0$, $z_2 = 0.005$ m, $z_3 = 0.01$ m, $z_4 = 0.04$ m [22].

A. Potential map

The potential in the m-th layer (m=1,2,...,n+1) is obtained via (9) through discretization of (10),

$$\phi_m(\mathbf{r}) = \frac{b^2}{\sigma_1}\sum_{k=1}^{PN} i_k G_m(\mathbf{r},\mathbf{r}_k), \quad \mathbf{r}_k \in S_p, \tag{28}$$

where $p = 1,2,...,P$, $1+(p-1)N \le k \le pN$, i_k is a component of the PN-dimensional vector i in (18) and G_m is the corresponding m-th layer Green's function.

The potential distribution and vector plot of the $x-y$ components of the electric field, depicted in Fig.2, is calculated for a four electrode array $P = 4$, $PN = 4\times400$=1600, m=1 and electrode size a=0.04 m. The map illustrates efficiently the complete excitation status of the biological tissue at the electrode plane $z_p = z_1 = 0$, $p = 1,2,3,4$. The electrode x-y spacings and the electrode potentials $\mathbf{V}$ are specified in Fig.2. The plot of the $x-y$ projection of the field vector $\mathbf{E}(\mathbf{r})$ in (2) is obtained through explicit (analytic) closed-form differentiation of $\phi(\mathbf{r})$ and $G_m(\mathbf{r},\mathbf{r}_k)$ in (28), i.e., term by term differentiation of the image series expansion.

B. Two-electrode configuration

We focus here on the dependence of electrode array and biological tissue interaction on the following three parameters: 1. electrode size, 2. electrode separation, 3. number of layers and their conductivities. The array configuration, therefore, is reduced to the simplest possible, i.e., a two-electrode system.

The numerical simulations carried out next signify the importance of an appropriate modeling of the tissue layers. Oversimplified models which utilize a reduced number of layers may result in an inaccurate simulation which may significantly obscure the real situation. Since our hybrid model can handle effectively n-layer problems, the decision whether a particular layer should be included in the model can be accurately made.

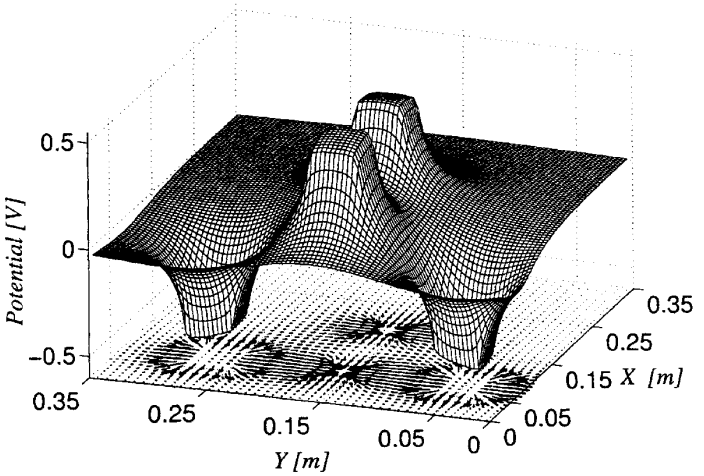

FIG. 2: Potential map and vector plot of the $x-y$ components of the electric field for a four-electrode array at $z{=}z_p{=}z_1{=}0$, p=1,2,3,4. The electrodes' size are a_p=0.04 m, their $x-y$ centers are $x{=}(x_1,x_2,x_3,x_4){=}$(0.1, 0.1, 0.1, 0.2)$[m]$, $y{=}(y_1,y_2,y_3,y_4){=}$ (0.05, 0.15, 0.25, 0.15)$[m]$, and their potentials are $\mathbf{V}$=(-0.5,0.5,-0.5,0.5) $[V]$, respectively.

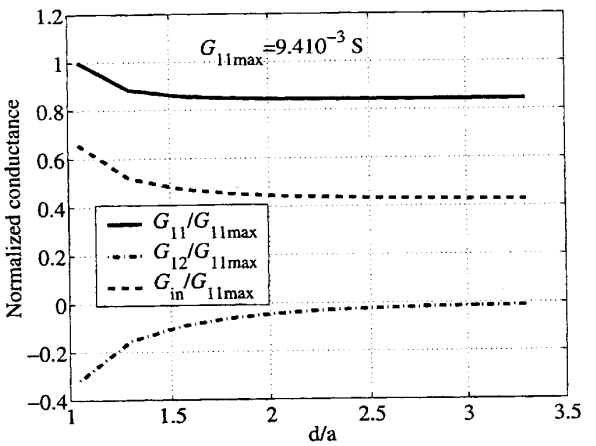

FIG. 3: Dependence of the normalized electrodes input conductance (Eq.(29)) and conductance matrix elements (Eq.(26)) on the normalized distances between the electrode centers.

a Calculations of the conductance matrix and the electrodes input admittance We focus herein on the evaluation of the conductance matrix elements G_{11} and G_{12} in (26) as well as the electrode input admittance G_{in}, given via,

$$G_{in} = \frac{I_2}{V_2 - V_1} = \frac{1}{2}(G_{11} - G_{12}), \qquad (29)$$

for the symmetrical two-electrode problem ($V_1 = -V_2 \Leftrightarrow G_{11} = G_{22}$, Eq.(16)). The dependence of G_{11}/G_{11max}, G_{12}/G_{11max} and G_{in}/G_{11max} on the electrodes' normalized center spacing $d/a \geq 1$, is given in Fig.3. Note that

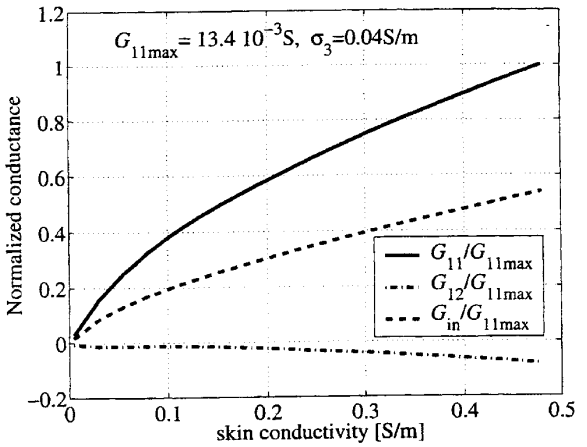

FIG. 4: Dependence of the normalized electrodes input conductance (Eq.(29)) and conductance matrix elements (Eq.(26)) on the second layer conductivity, σ_2, (skin).

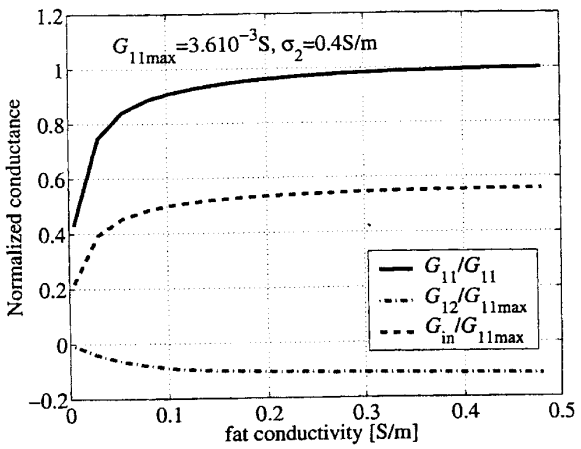

FIG. 5: Dependence of the normalized electrodes input conductance (Eq.(29)) and conductance matrix elements (Eq.(26)) on the third layer conductivity, σ_3 (fat).

for d/a >3, there is practically no interaction between the electrodes, i.e., G_{12} =0, and G_{11} reaches the single electrode limit. The normalized conductivity dependence on either σ_2 or σ_3 is depicted in Fig.4 and Fig.5, respectively. While the conductivities are strongly dependent on the skin layer conductivity (σ_2), that is in contact with the electrode array, the somewhat more moderate dependence on the fat layer conductivity (σ_3) cannot be ignored.

b Current distribution in the muscle layer The fundamental problem of field interaction with excitable tissue is investigated here for the muscle layer (σ_4). The x-component of the current density $\mathbf{j}(\mathbf{r})$ (Eq.(1)) is calculated in the muscle layer $\mathbf{r} = (x, 0, z)$, $z_3 \leq z \leq z_4$, for constant electrode currents and spacing ($I_1 = -I_2$=0.1 A and d =0.2 m, respectively) utilizing the image series ex-

pansions in Appendix A. Its dependence on the x-axis is depicted in Figs.6 and 7, for various electrode sizes (a=0.001 m, 0.005 m, 0.01 m, 0.04 m, setting $z = z_3$) and for two different conductivities of the lowermost layer ($\sigma_5 = \sigma_4$ or σ_5=0.07 S/m, setting; $a = 0.001m$ and $z = z_3$, $(z_3 + z_4)/2$, z_4), respectively.

The difference between the current density midway between the electrodes may be critical for whole muscle excitation. While the electrode size has (almost) no effect on the current distribution, midway between the electrodes (Fig.6), it has a strong influence on the maximal current density values, just beneath the electrode edge, due to a large or small electrode's distance to size ratio, respectively. Thus, it may be concluded that the main role of the electrode size is to reduce the maximum current density to below the safety threshold standard [1] by increasing the electrode area.

Furthermore, the selection σ_5=0.07 S/m enhances the current density due to the support of the lowermost layer (Figure 7), and the selection $\sigma_5 = \sigma_4$ reduces the current density due to the absence of the lowermost layer. Thus, disregarding the bone/fascia layer may lead to a painful error resulting in an underestimation of the inter-muscle current density. This important observation highlights once more the potential promise of the proposed method that can effectively handle layered medium problems with any number of layers.

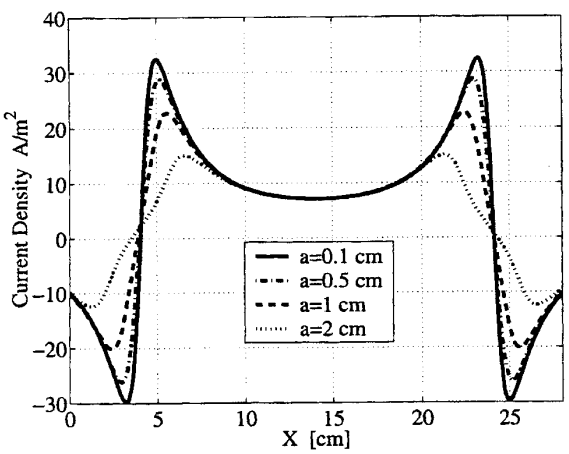

FIG. 6: Dependence of the current density $j_x(\mathbf{r})$ (Eq.(1))on x for various electrode sizes (setting r=$(x, 0, z_3)$ and d=0.2 m).

C. Isometric recruitment curve

The isometric recruitment curve (IRC) of a muscle is defined as the relation between the stimulus activation level and the output force when the muscle is held at a fixed length. The IRC curves depicted in Figs.8 and 9 are an extension, to finite size electrodes and to a five-

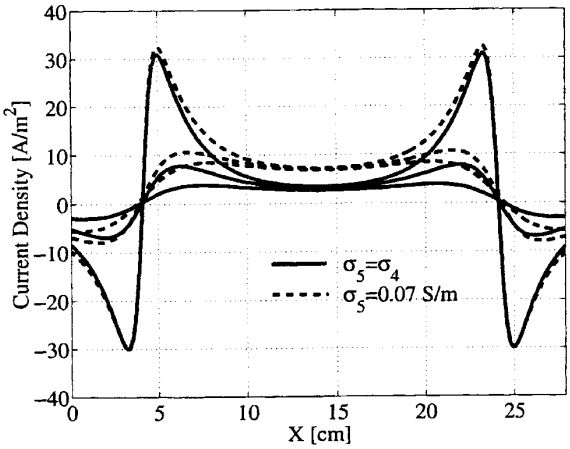

FIG. 7: Dependence of the current density $j_x(\mathbf{r})$ (Eq.(1)) on x for two different conductivities of the lowermost layer (setting z=[$z3$, $(z3 + z4)/2$, $z4$], a=0.001 m and d=0.2 m). Dashed line denotes σ=0.07 S/m and solid line denotes unbounded muscle σ=0.7 S/m

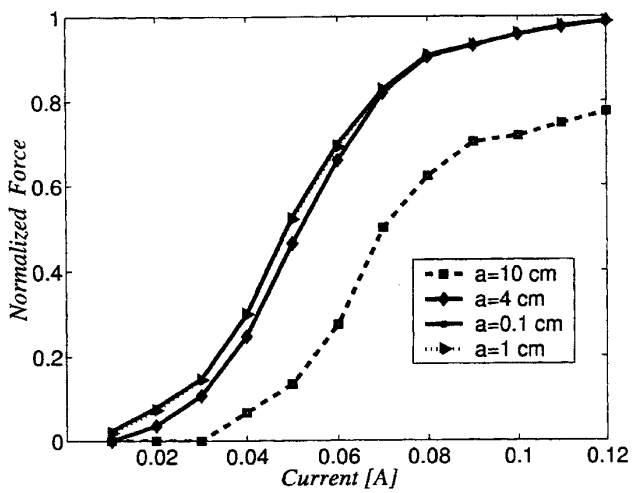

FIG. 8: Effect of electrode size on the IRC.

layer media (air, skin, fat, muscle, muscle boundary), of previous simulations [15].

Fig.8, presents the IRC for various electrode sizes (a = 0.001 m, 0.01 m, 0.04 m, 0.1 m). It should be noted that the 0.001 m electrode case gives a similar solution for both current density distribution and IRC problems as for the point-electrode case [15]. Despite the broad range of sizes (1 mm − 4 cm), the model shows no substantial effect of the electrode size on the IRC shape. However, for electrode sizes comparable to the width of the Quadriceps muscle (~10 cm), the IRC shifts toward the right side of the current axis and manifests an abrupt reduction of the maximal force. This is due to a more uniform current density, reducing the electrode current density below threshold.

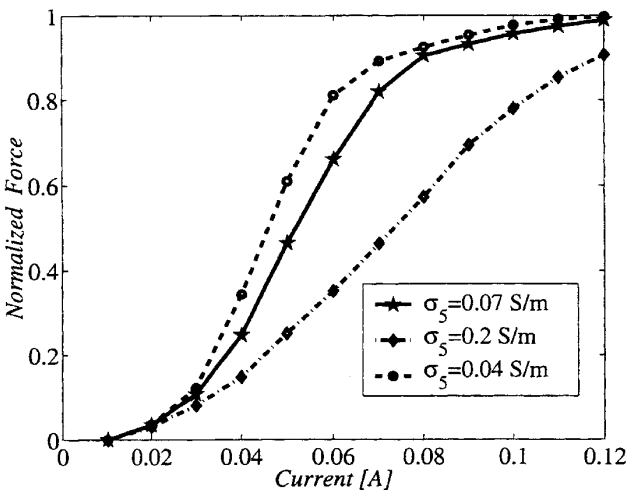

FIG. 9: Effect of the lowermost layer conductivity on the IRC.

The effect of different conductivities of the lowermost layer on the IRC is shown in Fig.9. The variations were from $\sigma_5 = \sigma_4$ (semi-infinite case) to $\sigma_5 = \sigma_3$ (poor conductive layer). The decrease in conductivity of the lowermost layer leads to an increase of the IRC slope and shifts the onset of the saturation region towards lower current values. The simulation results indicate, as expected and supported by the preceding discussion, that IRC are insensitive to the electrodes' size, however, the inclusion of the bone/fascia layer significantly increases the IRC slope.

ACKNOWLEDGMENTS

This study was supported in part by the Segal foundation.

REFERENCES

[1] REILLY, J.P., *Electrical Stimulation and Electropathology*, Cambridge University Press, 1992.

[2] REILLY, J.P., *Applied Bioelectricity*, New York, Springer-Verlag, 1998.

[3] RATTAY, F., *Modeling the excitation of fibres under surface electrodes* IEEE Trans.Biomed.Eng., vol.35, pp.199-202, 1988.

[4] WILEY, J.D., AND WEBSTER,J.G., *Analysis and control of the current distribution under circular dispersive electrode*, IEEE Trans.Biomed.Eng., vol.29, pp.381-385, 1982.

[5] JACKSON J.D., *Classical Electodynamics*, 3rd edition, Wiley, New York, 1999.

[6] RUBINSTEIN, J. T., SPELMAN, F. A., SOMA,M., AND SUSSERMAN M.F.*Current density profiles of surface mounted electrodes and recessed electrodes for neural prosthesis*, IEEE Trans.Biomed.Eng. 34, pp.864-874, 1987

[7] RODENHISER, K.L., AND SPELMAN,A. *A method for determining the driving currents for focused stimulation in the cochlea*, IEEE Trans.Biomed.Eng., vol.42, pp.337-342, 1995.

[8] TSAI, J.-Z., CAO,H., TUNGJITKUSOLMUN, S.E. WOO, J., VORPERIAN, V. R., AND WEBSTER, J.G., *Dependence of Apparent Resistance of Four-Electrode Probes on Insertion Depth* IEEE Trans.Biomed.Eng., vol.47, pp.41-48, 2000.

[9] GRILL,W.M., *Modeling the effects of electric fields on nerve fibers: Influence of tissue electrical properties*, IEEE Trans.Biomed.Eng., vol.46, pp.918-28, 1999.

[10] SOMERSALO,E.,CHENY,M.,ISAACSON,D., *Existence and uniqness for electrode models for electric current computed tomography*, SIAM J.Appl.Math, Vol.52, pp. 1023-40, 1992.

[11] KELLER, G.V., AND FRISCHKNECHT, F. C., *Electrical Methods in Geophysical Prospecting*, Oxford, Pergamon Press, 1970.

[12] WAIT, J.R.,*Geo-Electromagnetism*, Academic Press New York, 1982.

[13] CHOW, Y. L., AND SALAMA, M.M., *A simplified method for calculating the substation grounding grid resistance*, IEEE Trans. Power Delivery, vol. 9, pp. 736-742, 1994.

[14] LAGACE, P.J., HOULE, J.L., GERVAIS, Y., AND MUKHEDKAR, D., *Evaluation of the voltage distribution around toroidal HVDC ground electrodes in N-layer soils*, IEEE Trans. Power Delivery, vol.3, pp. 1573-1577, 1988.

[15] LIVSHITZ, L., EINZIGER P.D., AND MIZRAHI, J., *Current distribution in skeletal muscle activated by FES: Image-series formulation and isometric recruitment curve*, Ann.Biomed.Eng.vol.28, pp.1218-1228, 2000.

[16] EINZIGER, P.D. LIVSHITZ, L., AND MIZRAHI, J. *Rigorous image series expansions of quasistatic Green's functions for regions with planar stratification* submitted, IEEE Trans. Antenn. Propagat., 1999.

[17] HARRINGTON,R.F., *Field Computation by Moment Methods*, Macmillan, New York, 1968.

[18] HAUSE,H.A., MELCHER,J.R., *Electromagnetic Field and Energy*, Prentice-Hall International, Inc. Englewood Cliffs N.J., 1989.

[19] DWIGHT, H.B., *Tables of Integrals and Other Mathematical Data*, Macmillan Co., New York, 1947.

[20] KELLOGG, O.D., *Foundation of potential theory*, Dover Publication Inc., New York, 1953.

[21] BANCROFT, R., *Note on the moment method solution for a capacitance of a conducting flat plate*, IEEE Trans. Antenn. Propag., vol. 45, no.11, p.1704, 1997.

[22] FOSTER, K.R., AND SCHWAN, H.P.,*Dielectrical properties of tissues*, in POLK, C., AND POSTOW,

E.,, CRC Handbook of biological effects of electromagnetic field. CRC Press, Boca Raton, FL, pp.26-95, 1986.

[23] HUMMEL, J. N., *A theoretical study of apparent resistivity in surface potential methods*, Trans.Am.Inst.Min.Met.Eng., vol. 97, pp. 392-422, 1932.

[24] ROMAN,I. *An image analysis of multi-layer resisitivity problems*, Geophysics, vol.24, pp. 485-509, 1959.

[25] STEFANESCO, S. AND SCHLUMBERGER, C., AND M., *The distribution of electrical potential about a point electrode in an earth of horizontal, homogeneous, and isotropic beds*, J. Phys. Radium, vol.1, pp.130-141, 1930.

APPENDIX A: IMAGE SERIES EXPANSION OF GREEN'S FUNCTION IN LAYERED MEDIA

1. Integral representation

Setting $\mathbf{r}_p = (0,0,z')$ for the point-source coordinate leads to a circularly symmetric Green's function in (10) and (11) which can be expressed via a single spectral integral, known as the Fourier-Bessel representation [12],

$$G(\mathbf{r},\mathbf{r}_p) = \frac{1}{4\pi}\int_0^\infty g(z,z')J_0(\xi\rho)d\xi \qquad (A.1)$$

where J_0 is the Bessel function of the first kind and zero order, ρ is the radial coordinate and $g(z,z')$ is the characteristic Green's function, and given via [15], [16],

$$g_i(z,z') = \prod_{p=1}^{i} T_p(\xi)[e^{-\xi|z-z'|}+R_i e^{\xi(z+z')}], \quad z_{i-1}\le z\le z_i. \qquad (A.2)$$

The subscript i (p) denotes specific expressions or values that are valid in the i (p)-th layer, defined in (5). $R_i(\xi)$ and $T_i(\xi)$ in (A.2) are the reflection and the transmission coefficients, given recursively as

$$R_i(\xi) = \{K_i+\frac{[1-K_i^2]R_{i+1}(\xi)e^{2\xi z_i}}{1+K_iR_{i+1}(\xi)e^{2\xi z_i}}\}e^{-2\xi z_i}, \quad R_{n+1}(\xi)=0, \qquad (A.3)$$

and

$$T_i(\xi) = \frac{1+K_{i-1}}{1+K_{i-1}R_i(\xi)e^{2\xi z_{i-1}}}, \quad T_1(\xi)=1, \qquad (A.4)$$

where K_i denotes the intrinsic reflection coefficient of the i-th interface,

$$K_i = \frac{\sigma_i-\sigma_{i+1}}{\sigma_i+\sigma_{i+1}}, \quad K_0=0, \quad \sigma_0=0. \qquad (A.5)$$

2. Image series expansions via the loop operator

The finite binomial series expansion, containing M terms and a remainder,

$$\frac{1}{(1-x)^{N+1}} = \sum_{m=0}^{M}\binom{m+N}{m}x^m + \sum_{p=0}^{N}\binom{M+N+1}{M+p+1}\frac{x^{M+p+1}}{(1-x)^{p+1}}, \qquad (A.6)$$

is a vital tool for the image series expansion of (A.2) and consequently (A.1). The series converges as $M\to\infty$, for all $|x|<1$. Image series representations has been obtained upon repeatedly expanding both the reflection and the transmission coefficients in (A.3) and (A.4), respectively, in finite binomial series as outlined in (A.6) [16].

Unfortunately, the representations become quite cumbersome as the number of layers increases (e.g. [23], [24],[25]). More succinct representations can be obtained by introducing the notation $\coprod$ for the loop operator, defined via,

$$\sum_{n_1=m_1}^{M_1} h_1(n_1)\sum_{n_2=m_2(n_1)}^{M_2(n_1)} h_2(n_1,n_2)\ldots\sum_{n_q=m_q(n_1,\ldots,n_{q-1})}^{M_q(n_1,\ldots,n_{q-1})} h_q(n_1,\ldots,n_q) =$$
$$\sum_{n_1=m_1}^{M_1}\sum_{n_2=m_2(n_1)}^{M_2(n_1)}\cdots\sum_{n_q=m_q(n_1,\ldots,n_{q-1})}^{M_q(n_1,\ldots,n_{q-1})} h_1(n_1)\ldots h_q(n_1,\ldots,n_q) =$$
$$\coprod_{j=1}^{q}\sum_{n_j=m_j(n_1,n_2,\ldots,n_{j-1})}^{M_j(n_1,n_2,\ldots,n_{j-1})} h_j(n_1,n_2,\ldots,n_j), \qquad (A.7)$$

where q denotes the overall number of the nested cycles (layers). The upper and the lower summation limits of the j-th cycle, denoted by $M_j(n_1,n_2,\ldots,n_{j-1})$ and $m_j(n_1,n_2,\ldots,n_{j-1})$, respectively, depend on the preceding $n_1,n_2,\ldots,n_{j-1}$ indices, whereas the function $h_j(n_1,n_2,\ldots,n_j)$, evaluated in the j-th cycle, depends on all the $n_1,n_2,\ldots,n_j$ indices. For $q<j$ the loop operator is defined as $\coprod_{j=1}^{q}=1$.

While repeatedly expanding (A.3) and (A.4) via (A.6), the characteristic Green's function $g_i(z,z')$ is most conveniently decomposed into two finite image series expansions, $g_i^+(z,z')$ and $g_i^-(z,z')$, and two corresponding remainder terms $\gamma^+(z,z')$ and $\gamma^-(z,z')$,

$$g_i(z,z') = \prod_{p=1}^{i-1}[1+K_p][g_i^+(z,z')+g_i^-(z,z')] + \sum_{j=1}^{n-1}\frac{\prod_{k=1}^{i-1}(1+K_k)}{\prod_{k=j+1}^{i-1}[1+K_kR_{k+1}(\xi)e^{\xi z_k}]} \times[\gamma^+_{i,M_1,\ldots,M_j}(z,z')+\gamma^-_{i,M_1,\ldots,M_j}(z,z')]. \qquad (A.8)$$

where the index j represents summation over all layers, and M_j is related to the number of images accounted

for in the j-th layer and are contained in $g_i^+(z,z')$ and $g_i^-(z,z')$. Note that, $g_i^+(z,z')$ and $g_i^-(z,z')$ correspond to the transmitted and reflected image contributions, respectively, whereas $\gamma^+(z,z')$ and $\gamma^-(z,z')$ collectively account for the truncated transmitted and reflected image contributions.

The image series representations, utilizing the loop operator for $i>1$, is summarized herein. The representations for $i=1$ can be expressed in term of the $i=2$ expansions and thus given subsequently.

$$g_i^{\pm}(z,z') = \coprod_{j=1}^{n-1}\Bigg[\sum_{l_{j-1}=0}^{m_1+\ldots+m_j-l_1-\ldots-l_{j-2}+\eta^{\pm}_{i,j,1}}\sum_{m_j=0}^{M_j} \times \binom{m_1+\ldots+m_{j-1}-l_1-\ldots-l_{j-2}+\eta^{\pm}_{i,j,1}}{l_{j-1}} \times \binom{m_1+\ldots m_j-l_1-\ldots-l_{j-1}+\eta^{\pm}_{i,j,1}-1+\mu_{i,j}}{m_j} \times (-K_j)^{m_j}K_j^{l_{j-1}}(1-K_j^2)^{m_1+\ldots+m_{j-1}-l_1-\ldots-l_{j-1}+\eta^{\pm}_{i,j,1}} \times e^{-2\xi(z_{j+1}-z_j)(m_1+\ldots+m_j-l_1-\ldots-l_{j-1}+\eta^{\pm}_{i,j,1})} \times K_n^{m_j-l_{j-1}}\Bigg]K_n^{\eta^{\pm}_{i,2,1}-\eta^{\pm}_{i,n,0}}e^{-\xi(z\mp z')}, \tag{A.9}$$

where the summation factor $\eta^{\pm}_{i,j,k}$,

$$\eta^{+}_{i,j,k}=0, \quad \eta^{-}_{i,j,k}=k-\mu_{i,j}, \tag{A.10}$$

is expressed via the discrete step function $\mu_{i,j}$,

$$\mu_{i,j}=\begin{cases}1, & i>j\\ 0, & i\le j.\end{cases} \tag{A.11}$$

The equalities $l_{-1}=l_0=0$, $m_0=0$, are also adapted here. The individual truncation error, associated with the j-th layer (M_j) and depending on the preceding j-1 layers ($M_1, M_2, ..., M_{j-1}$), is given as,

$$\gamma^{\pm}_{i,M_1,\ldots,M_j}(z,z') = \coprod_{k=2}^{j}\Bigg[\sum_{m_{k-1}=0}^{M_{k-1}} \times \binom{m_1+\ldots+m_{k-1}-l_1-\ldots-l_{k-1}+\eta^{\pm}_{i,k,1}-1+\mu_{i,j}}{m_{j-1}} \times \sum_{l_{k-1}=0}^{m_1+\ldots+m_{k-1}-l_1-\ldots-l_{k-2}+\eta^{\pm}_{i,k,1}} \times \binom{m_1+\ldots+m_{k-1}-l_1-\ldots l_{j-2}+\eta^{\pm}_{i,k,1}}{l_{k-1}} \times(-K_{k-1})^{m_{k-1}}K_k^{l_{k-1}}(1-K_k^2)^{m_1+\ldots+m_{k-1}-l_1-\ldots-l_{k-1}+\eta^{\pm}_{i,k,1}} \times e^{-2\xi(z_k-z_{k-1})(m_1+\ldots+m_{k-1}-l_1-\ldots-l_{k-2}+\eta^{\pm}_{i,k,1})} \times [R_{j+1}(\xi)e^{2\xi z_j}]^{m_{k-1}-l_{k-1}}\Bigg] \times [R_i(\xi)e^{2\xi z_j}]^{-\eta^{\pm}_{i,j,0}} \sum_{p=0}^{m_1+\ldots+m_{j-1}-l_1-\ldots-l_{j-1}+\eta^{\pm}_{i,j,1}-1+\mu_{i,j}} \times \binom{M_j+m_1+\ldots+m_{j-1}+1-l_1-\ldots-l_{j-1}+\eta^{\pm}_{i,j,0}+\mu_{i,j}}{M_j+p+1} \times \frac{[-K_je^{2\xi z_j}R_{j+1}(\xi)]^{M_j+p+1}}{[1+K_jR_{j+1}(\xi)e^{2\xi z_j}]^{p+1}}e^{-(z\mp z')}. \tag{A.12}$$

Substituting (A.8) into (A.1) and utilizing the Weber-Lipschitz identity [12]

$$\int_0^{\infty}e^{-\xi|z-z'|}J_0(\xi\rho)\mathrm{d}\xi=\frac{1}{|\mathbf{r}-\mathbf{r}_p|}, \tag{A.13}$$

results in an image series expansion for $G_i(\mathbf{r},\mathbf{r}_p)$

$$G_i(\mathbf{r},\mathbf{r}_p)=\frac{1}{4\pi}\{\prod_{p=1}^{i-1}(1+K_p)[G_i^+(\mathbf{r},\mathbf{r}_p)+G_i^-(\mathbf{r},\mathbf{r}_p)]+\Gamma_i(\mathbf{r},\mathbf{r}_p)\}, \tag{A.14}$$

where

$$G_i^{\pm}(\mathbf{r},\mathbf{r}_p) == \coprod_{j=1}^{n-1}\Bigg[\sum_{l_{j-1}=0}^{m_1+\ldots+m_j-l_1-\ldots-l_{j-2}+\eta^{\pm}_{i,j,1}}\sum_{m_j=0}^{M_j} \times \binom{m_1+\ldots+m_{j-1}-l_1-\ldots-l_{j-2}+\eta^{\pm}_{i,j,1}}{l_{j-1}} \times \binom{m_1+\ldots m_j-l_1-\ldots-l_{j-1}+\eta^{\pm}_{i,j,1}-1+\mu_{i,j}}{m_j} \times (-K_j)^{m_j}K_j^{l_{j-1}}(1-K_j^2)^{m_1+\ldots+m_{j-1}-l_1-\ldots-l_{j-1}+\eta^{\pm}_{i,j,1}} \times K_n^{m_j-l_{j-1}}\Bigg]\frac{K_n^{\eta^{\pm}_{i,2,1}-\eta^{\pm}_{i,n,0}}}{[x^2+y^2+(z-z'^{\pm})^2]^{1/2}}, \tag{A.15}$$

$$z'^{\pm} = \pm\,[z' - 2\sum_{j=1}^{n-1}(z_{j+1} - z_j) \times (m_1 + ... + m_j - l_1 - ... - l_{j-1} + \eta^{\pm}_{i,j,1})], \tag{A.16}$$

and a remainder term $\Gamma(\mathbf{r}, \mathbf{r}_p)$ representing a collective image, i.e., summation over all the image series terms that are not included in the finite image series (A.15). Following [16] $\Gamma_{M_1,...,M_j}(\mathbf{r}, \mathbf{r}_p)$ is evaluated asymptotically (end-point integration) for $M_j \to \infty$, $j = 1, 2, ..., n-1$, yielding,

$$\Gamma_i(\mathbf{r}, \mathbf{r}_p) \sim \tilde{\Gamma}_i(z, z') = \sum_{j=1}^{n-1} \frac{\prod_{k=1}^{i-1}(1 + K_k)}{\prod_{k=j+1}^{i-1}[1 + K_k R_{k+1}(0)]} \times [\tilde{\Gamma}^{+}_{i,M_1,...,M_j}(z, z') + \tilde{\Gamma}^{-}_{i,M_1,...,M_j}(z, z')]. \tag{A.17}$$

The asymptotic truncation error $\tilde{\Gamma}_{M_1,...,M_j}(z, z')$ is expressed as,

$$\begin{aligned}
\tilde{\Gamma}^{\pm}_{i,M_1,...,M_j}(z, z') = & \prod_{k=2}^{j} \Bigg[\sum_{m_{k-1}=0}^{M_{k-1}} \times \binom{m_1 + ... + m_{k-1} - l_1 - ... - l_{k-1} + \eta^{\pm}_{i,k,1} - 1 + \mu_{i,j}}{m_{j-1}} \\
& \times \sum_{l_{k-1}=0}^{m_1+...+m_{k-1}-l_1-...-l_{k-2}+\eta^{\pm}_{i,k,1}} \times \binom{m_1 + ... + m_{k-1} - l_1 - ... l_{j-2} + \eta^{\pm}_{i,k,1}}{l_{k-1}} \\
& \times (-K_{k-1})^{m_{k-1}} K_k^{l_{k-1}} (1 - K_k^2)^{m_1+...+m_{k-1}-l_1-...-l_{k-1}+\eta^{\pm}_{i,k,1}} \\
& \times [R_{j+1}(0)]^{m_{k-1}-l_{k-1}} \Bigg] \\
& \times [R_i(0)]^{-\eta^{\pm}_{i,j,0}} \sum_{p=0}^{m_1+...+m_{j-1}-l_1-...-l_{j-1}+\eta^{\pm}_{i,j,1}-1+\mu_{i,j}} \\
& \times \binom{M_j + m_1 + ... + m_{j-1} + 1 - l_1 - ... - l_{j-1} + \eta^{\pm}_{i,j,0} + \mu_{i,j}}{M_j + p + 1} \\
& \times \frac{[-K_j R_{j+1}(\xi)]^{M_j+p+1}}{[1 + K_j R_{j+1}(0)]^{p+1}[z - Z^{\pm}]},
\end{aligned} \tag{A.18}$$

where

$$R_{j+1}(0) = (\sigma_{j+1} - \sigma_{n+1})/(\sigma_{j+1} + \sigma_{n+1}). \tag{A.19}$$

$$Z^{\pm} = \pm\{z' - 2\sum_{k=2}^{j}[(z_k - z_{k-1})(m_1 + ... + m_{k-1} - l_1 - ... - l_{k-2}) + (z_{j+1} - z_j) \times (m_{k-1} - l_{k-1} + M_j + p + 1 + \eta^{\pm}_{i,k,1}]\} \tag{A.20}$$

The following uppermost layer functions ($i = 1$); $g_1(z, z')$, $\gamma_1(z, z')$, $G_1(\mathbf{r}, \mathbf{r}_p)$, $\Gamma_1(\mathbf{r}, \mathbf{r}_p)$, and $\tilde{\Gamma}_1(z, z')$ are related to the second layer "reflection" functions ($i = 2$); $g_2^{-}(z, z')$, $\gamma_2^{-}(z, z')$, $G_2^{-}(\mathbf{r}, \mathbf{r}_p)$, $\Gamma_2^{-}(\mathbf{r}, \mathbf{r}_p)$, and $\tilde{\Gamma}_2^{-}(z, z')$, respectively:

$$g_1(z, z') = (1 - K_1) g_2^{-}(z, z') + e^{-\xi|z-z'|} + K_1 e^{\xi(z+z')} + \gamma_1(z, z'), \tag{A.21}$$

$$\gamma_1(z, z') = (1 - K_1)\gamma_2^{-}(z, z'), \tag{A.22}$$

$$G_1(\mathbf{r}, \mathbf{r}_p) = \frac{1}{4\pi}[(1 - K_1) G_2^{-}(\mathbf{r}, \mathbf{r}_p) + \frac{1}{|\mathbf{r} - \mathbf{r}_p|} + \frac{K_1}{|\mathbf{r} + \mathbf{r}_p|} + \Gamma_1(\mathbf{r}, \mathbf{r}_p)], \tag{A.23}$$

$$\Gamma_1(\mathbf{r}, \mathbf{r}_p) = (1 - K_1)\Gamma_2^{-}(\mathbf{r}, \mathbf{r}_p), \tag{A.24}$$

$$\tilde{\Gamma}_1(z, z') = (1 - K_1)\tilde{\Gamma}_2^{-}(z, z'). \tag{A.25}$$

In n-layered media, the finite expansion in (A.15) converges, if at least n-1 of the intrinsic reflection coefficients $|K_i|$, $1 \le i \le n$, are less than unity [16].